Journal of Materials Chemistry A

Structural Mapping and Tuning Mixed Halide Ions in Amorphous Sulfides for Fast Li-Ion Conduction and High Deformability

Journal:	*Journal of Materials Chemistry A*
Manuscript ID	TA-ART-12-2022-009585.R1
Article Type:	Paper
Date Submitted by the Author:	25-Feb-2023
Complete List of Authors:	Kim, Ji-Su; Korea Institute of Science and Technology, Energy Materials Research Kim, Young Jung; Korea Institute of Science and Technology, Energy Materials Research Han, Daseul; Dongguk University - Seoul Campus Nam, Kyung-Wan; Dongguk University-Seoul, Department of Energy and Materials Engineering Kwon, Gihan; Brookhaven National Laboratory, Photon Science Division - National Synchrotron Light Source II Heo, Tae Wook; Lawrence Livermore National Laboratory, Materials Science Division Jung, Hun-Gi; Korea Institute of Science and Technology (KIST), Center for Energy Storage Research Yoon, Kyung Joong; Korea Institute of Science and Technology, High-Temperature Energy Materials Center Kim, Hyoungchul; Korea Institute of Science and Technology, High-Temperature Energy Materials Research Center

Structural Mapping and Tuning Mixed Halide Ions in Amorphous Sulfides for Fast Li-Ion Conduction and High Deformability

Ji-Su Kim,[a] Young Jung Kim, [a] Daseul Han,[b] Kyung-Wan Nam,[b] Gihan Kwon,[c] Tae Wook Heo,[d] Hun-Gi Jung,[e] Kyung Joong Yoon,[a] Hyoungchul Kim[ad*]

[a]*Energy Materials Research Center, Korea Institute of Science and Technology, Seoul 02792, Republic of Korea*

[b]*Department of Energy and Materials Engineering, Dongguk University, Seoul 04620, Republic of Korea.*

[c]*National Synchrotron Light Source II, Brookhaven National Laboratory, Upton, NY 11973, United States.*

[d]*Materials Science Division, Lawrence Livermore National Laboratory, Livermore, CA 94550, United States.*

[e]*Energy Storage Research Center, Korea Institute of Science and Technology, Seoul 02792, Republic of Korea.*

*Corresponding author. E-mail address: hyoungchul@kist.re.kr (H. Kim)

† Electronic Supplementary Information (ESI) available: See DOI: 10.1039/x0xx00000x

Amorphous sulfides are among the most promising candidates for solid electrolytes (SEs) owing to their excellent deformability and acceptable Li-ion conductivity (σ_{ion}) at room temperature. However, the complex atomic structure of these amorphous materials without long-range ordering results in a lack of structural understanding and difficulties in tuning material properties. In this study, we performed structural mapping of the glassy sulfide SEs composed of various anion clusters using a combinatorial atomic level analysis of synchrotron X-ray-based pair distribution function (PDF) and reverse Monte-Carlo (RMC) methods, demonstrating the potential to tune σ_{ion} in glass SEs. First, we prepared a new glassy sulfide with a mixed anion framework of two halogens (Br and I) as atomic anions, with PS_4^{3-} molecular anions in a Li_2S-P_2S_5-based glass SE. At a specific Br content, $[(Li_2S)_{0.658}(LiI_{0.9}LiBr_{0.1})_{0.342}]_{0.825}[P_2S_5]_{0.175}$ recorded a σ_{ion} of 2.27 mS cm^{-1}, the highest value of any glass sulfides reported to date; however, its elastic modulus was still suppressed to 14.48 GPa. PDF and RMC calculations successfully provided structural mapping of anion clusters, including two halogens. Molecular dynamics simulations each composition confirmed that flexible coordination caused by the rattling of small polarizable Br ions in the mixed halogens of glassy SEs contributed to the superior σ_{ion}. Our results may provide new insights into the design of superior glassy SEs that play key roles in all-solid-state batteries requiring fast Li-ion conduction and high deformability.

Introduction

Amorphous matter, resembling a fluid phase with an irregular and non-equilibrium arrangement of atoms from an atomistic viewpoint but having a physical form of a solid phase from a macroscopic viewpoint, is one of the most interesting material structures.[1–8] Through a combination of various glass formers and network modifiers, this material offers the possibility of infinite compositional diversity and property improvements without structural limitations.[1–11] Consequently, amorphous materials have been utilized in various industrial applications and are still being studied as promising next-generation materials.[9–11] In electrochemical phenomena and reactions involving mass transport, such as ions, this structure has various advantages due to its thermodynamically metastable phase.[7,8] For example, many amorphous features, such as an open structure with large internal free space, isotropic bulk properties, and various types of defects, can significantly benefit ion migration.[12,13] However, the limited understanding of amorphous structures caused by the absence of long-range ordering hampers precise property control and novel structure design.[7,8] Relevant research in this field still relies on trial-and-error approaches. In fact, because the practical methodology for preparing an amorphous material, *i.e.*, amorphization, utilizes fast cooling or undercooled solidification of a molten (or glassy) mixture, structural uncertainty and complexity are inevitable. Therefore, the structural understanding of these materials remains a major challenge for tuning their physical and chemical properties, despite remarkable advances in computational science and analytical techniques in recent years.[7,8,14,15]

For example, in the early stage of solid electrolyte (SE) research, considerable efforts were made to achieve the aforementioned advantages of amorphous materials, leading the research and making a significant milestone. In particular, the sulfur-based anionic framework with low electronegativity has been recognized as a promising glass structure with

excellent cation mobility.[16–19] Furthermore, in the cell structure of all-solid-state batteries (ASSBs), which require a dense and reliable solid-to-solid interface structure, the excellent deformability of sulfide SEs offers facile densification of material interfaces by cold pressing at room temperature (*T*).[19–21] Considering a typical cathode active material with many crystallographic anisotropies, including a layered structure, the isotropic properties of glassy sulfide SEs are another advantage for material compatibility and process flexibility at the interface with the active material.[22,23] Owing to their reasonable ionic conductivity (σ_{ion}), excellent deformability, and aforementioned isotropic features, glassy sulfide SEs are widely used in ASSB applications.[19–21] The market demand to move toward advanced ASSBs with long lifetime and high energy density comparable to those of liquid electrolytes is growing, but the current state-of-the-art SEs still have a huge gap to bridge.[24,25] Therefore, improving the σ_{ion} of glassy sulfide SEs while maintaining their inherent mechanical properties, *e.g.*, elastic modulus (*E*) of approximately 20 GPa, which is very low for other inorganic materials, is important.[19–21] However, there are few acceptable and high-caliber methods for tuning a glassy sulfide SE. Structural understanding of the factors affecting σ_{ion} and mechanical properties of glassy materials without long-range ordering is lacking, and appropriate analysis techniques for these materials are limited. Moreover, computational approaches, which have undergone recent advances, are still inadequate for simulating the structural uncertainty of glassy materials without considerable computational and time costs.[26,27] These limitations severely hinder the development of superior glassy sulfide SEs based on a systematic structural understanding and prediction. In contrast, some studies dealing with crystalline sulfide SEs, which are relatively easy to analyze structurally, have reported that ion conduction and/or mechanical properties can be controlled by tuning an anion framework, mixing anion clusters, and other means.[28–33]

Therefore, in this study, we report superior glass SEs with fast Li-ion conduction and high deformability by achieving systematic structural understanding and prediction via combinatorial atomic level analyses. First, we analyzed the structural changes in glassy sulfides varying the type and content of anion species. Using synchrotron X-ray based pair distribution function (PDF), reverse Monte-Carlo (RMC), and density functional theory (DFT) methods, the relevant glassy structures were comprehensively reconstructed, and anionic framework was successfully mapped. Based on these simulated structures, we determined the contributions of anionic structure to Li-ion conduction and mechanical properties. Finally, new glassy sulfide SEs with high σ_{ion} and low E were proposed by introducing and mixing highly polarizable atomic halogen (X) anions that provide complementary functions to existing molecular anion clusters.

Results and discussion

Conventional Li-ion conducting framework in glass sulfide SEs

Ion conductive glassy materials consist of various glass formers and network modifiers.[1,6,7,24,25] Their physical and chemical properties considerably depend on the type, charge state, shape, and mixing ratio of each ion cluster.[30–33] In particular, for several cation conductors with high industrial impact (*e.g.*, Li^+ and Na^+), various anion clusters, as shown in Fig. 1a, can be employed: monatomic [*e.g.*, halogens such as F^-, Cl^-, Br^-, and I^-], diatomic (*e.g.*, CN^- and OH^-), molecular (*e.g.*, PS_4^{3-}, BH_4^-, and SO_3^{2-}), and polymerized anion clusters in which two or more of them are combined. Given their unique structural features, such as the absence of long-range ordering, glass systems that enable extensive use and combinations of these diverse anion clusters are suitable for controlling σ_{ion}. The most widely studied Li-ion conductive glass was developed based on the binary system of Li_2S-P_2S_5 (LP), and its paddle wheel and hopping mechanism with non-bridging S and PS_4^{3-} anion clusters

have also been proposed (see Fig. 1b).[34,35] Later, a ternary system based on Li_2S-P_2S_5-LiI (LPI) was proposed and showed significantly higher σ_{ion} than the binary system.[16] In this case, I^- halogen ions play an important role as atomic anions in improving Li-ion transport via the hopping mechanism.[16] Figure 1c shows a colour contour plot of the σ_{ion} results as a function of the mixing ratio of three constituent materials in this LPI ternary system. In particular, the orange-red region ($0.51 < Li_2S < 0.59$, $0.12 < P_2S_5 < 0.20$, and $0.24 < LiI < 0.36$) is where σ_{ion} is maximized (> 1.50 mS cm^{-1}). We found that LPI3, *i.e.*, $[(Li_2S)_{0.658}(LiI)_{0.342}]_{0.825}(P_2S_5)_{0.175}$, within this region has the highest σ_{ion} of approximately 1.96 mS cm^{-1}. Notably, all acronyms, chemical formulas, and measured conductivities of the SE materials tested in this study are summarized in Table 1. From the crystallographic features of glass, this result demonstrates the contribution of anion clusters to the σ_{ion} enhancement. However, the understanding of these glassy features is still in its early stages and must be furthered by applying advanced atomic level analysis. For example, conventional bulk analyses, such as X-ray diffraction (XRD) and X-ray photoelectron spectroscopy (XPS) presented in Figs. 1d and 1e, are very useful tools for analyzing the crystal structure and bonding characteristics of materials; however, they have limitations in the analysis of glassy materials. No noticeable change as a function of LiI content was found in the crystalline phase or bonding structure, whereas a large σ_{ion} change due to the introduction of LiI was experimentally observed (see Fig. 1c). The observation of anion locations and bond changes between ions is important for the analysis of ion transport characteristics. Therefore, the development of advanced atomic analysis techniques capable of directly observing and simulating these glass features are necessary, considering the limitations of such conventional bulk analysis.

Anomalous Li-ion conduction in glass sulfide SEs with mixed halides

To expand the σ_{ion} tuning strategies of glassy SEs through mixed anions, as discussed in the previous section, we devised a novel glassy material with two halogens as atomic anions (Br^- and I^-) with intrinsic PS_4^{3-} molecular anions, and we attempted to understand the complex mixed anion structure. The newly introduced halogen atomic ion Br^-, an isovalent ion to the existing I^- ion, has several beneficial effects on glassy structure modification. This isovalent anion mixing does not disturb or rearrange the charge distribution; however, it provides a complementary ion pathway due to its smaller ionic radius compared to conventional I^- and PS_4^{3-} anions. Figure 2a shows the results of laboratory XRD analysis for several LiBr substituted LPI3 (denoted as LPI3-Br) samples. As mentioned in the Materials and Methods section, the same synthesis conditions as those of the LPI series were applied, and we confirmed that all as-milled LPI3-Br samples had an amorphous phase, regardless of the amount of LiBr (see Fig. S1, ESI†). Figure 2b presents the variations in σ_{ion} for the quaternary system of the LPI3-Br series as a function of LiBr content, which shows a relatively anomalous compositional dependence. σ_{ion} increased rapidly at an LiBr content of approximately 10%, whereas further increase, gradually decreased σ_{ion} thereafter. The maximum σ_{ion} was recorded to be approximately 2.27 mS cm^{-1} for the LPI3-Br10 sample, which is an increase of 15.8% compared to the existing LPI3 sample and is one of the highest σ_{ion} results for sulfide-based glassy SEs reported to date.[19] Considering the amorphous features of glassy structures, we acknowledge that a higher LiI content with a larger ion radius and greater polarizability is more favourable for phonon softening and ion hopping.[37] However, the sharp increase in σ_{ion} at an LiBr content of approximately 10% is an intriguing result, different from the well-known ion transport phenomena in glass SEs.[16,34,35] In addition, activation energy (E_a) analysis was very useful for verifying whether the Li-ion transport mechanism changes in the LPI3-Br series. As shown in Fig. 2c, the Arrhenius plot for the LPI3-Br series shows that the measured E_a of LPI3-Br10 is 0.18 eV, which is lower than that

of any sulfide-based glass SEs, including LP75 (0.24 eV) and LPI3 (0.20 eV). The LPI3-Br10 sample with the lowest E_a had the highest σ_{ion} at room temperature. Thus, the suppressed E_a observed in the LPI3-Br10 sample further verifies that a new Li-ion migration mechanism is constructed via the introduction of Br^-.

Analysis of mechanical properties of LPI3-Br series

Figure 3a shows the variation in several mechanical properties [elastic constants such as *E*, shear (*G*), and bulk modulus (*B*)] and Poisson's ratio (*v*) in the LPI3-Br series. The mechanical properties of the LPI3-Br series were measured using the ultrasonic pulse-echo (USPE) method, and the measured shear and longitudinal wave velocities (V_S and V_L, respectively) were converted into several elastic constants, as listed in Table 2. We found no significant variation in the elastic constants with composition change in the LPI3-Br series. Despite the substitution of LiBr (38 GPa) with a higher *E* compared to LiI (27 GPa), the substitution of a small amount of LiBr did not affect the overall elastic constants in the LPI3-Br series.[19] The measured *E*, *B*, and *G* in LPI3-Br10 with the highest σ_{ion} were 14.48, 12.04, and 5.57 GPa, respectively, similar to those of other LPI3-Br series. The obtained *E* and σ_{ion} of LPI3-Br10 were compared with those reported for crystalline (here, Li_6PS_5Cl, one of the most promising crystalline SEs owing to its high σ_{ion} and good phase stability) or glassy SEs (LP series and LPI3-Br10), as shown in Fig. 3b. Most glassy SEs have remarkable deformability, whereas Li_6PS_5Cl crystallized at an elevated *T* has high σ_{ion} and poor deformability. The LP series of glassy SEs have been reported to be used as SEs due to their higher deformability compared to crystalline SE.[19,36] However, their poor σ_{ion} (0.01–0.5 mS cm^{-1}) has limited their applications.[19] Surprisingly, our LPI3-Br series maintained a lower *E* than the LP series despite the improved σ_{ion}. From these results, we confirmed that LPI3-Br10 composed of mixed anions can overcome the limitations of ionic transport and mechanical properties in glassy SEs.

Structural mapping of LPI3-Br series using RMC simulation

As previously reported, the properties of Li-ion transport in SEs are determined by their atomic structure.[31–33] From this viewpoint, several studies on the Li-ion conduction mechanism based on the analysis of anion framework have been conducted in crystalline SEs, both experimentally and theoretically.[31–33,38] As mentioned above, however, the conventional bulk analysis approaches are insufficient to isolate key physical and chemical factors that determine ionic conduction mechanisms of glassy SEs, necessitating the advanced structural understanding of disordered atomistic configurations. Accordingly, in this study, the advanced atomic analyses of LPI3-Br series were performed by applying atomic PDF analysis and RMC simulation. In the RMC simulation, the PDFs [$g(r)$] of the LPI3-Br series were obtained through the total structure factor $S(q)$ via the PDF experiments (see Fig. S2, ESI†). Based on the PDF analysis of the deconvoluted peaks, the cut-off distances of the first and second nearest neighbours were determined to perform the RMC simulation. The constraints and cut-off distances used for the RMC simulation are summarized in Methods section and Table S1 (ESI†). All simulations were repeated until the goodness-of-fit indicator (here, weighted residual error R_w) is converged. As shown in Fig. 4a, the calculated R_w of the LPI3-Br series was less than 5%, indicating that the bond distribution of the anion polyhedron and halogen ion was in general agreement with the experimental results. Based on the calculated $S(q)$ using RMC simulation, the PDFs and atomic structures of the LPI3-Br series were reconstructed, as shown in Figs. 4b and 4c; detailed information on the distribution of atoms and bonds is shown in Fig. S3 (ESI†). Examining the PDF results up to 20 Å, no noticeable peak was observed above 5 Å. Therefore, all samples exhibit highly disordered structures, incorporating short-range ordering only up to approximately 5 Å. We also confirmed that the short-range ordered bond distances (*e.g.,* P-S, Li-S, Li-X, and S-S) as the first nearest neighbours were well-reproduced in the PDF results. However, the

distribution of anion polyhedron and bond distance, such as second-nearest neighbours within 3.5–5 Å, deviate slightly from the experimental results. Despite these drawbacks, considering the fitting accuracy of the $S(q)$ and the acceptable PS_4^{3-} framework, we concluded that the atomic structures of the LPI3-Br series derived from the RMC simulation well-reproduced the experimental results. In Fig. 4c, the visualized atomic structures displaying the ion cluster distribution (PS_4^{3-} tetrahedron, LiI, and LiBr) for the LPI3-Br series indicate that the random distribution of ions in the long range was achieved while maintaining the short-range bonding in the entire cell structure.

Prediction of Li-ion transport and mechanical properties in LPI3-Br series

Based on the structural mapping results of the LPI3-Br series obtained using the RMC simulation, *ab initio* molecular dynamics (AIMD) simulations were performed to understand the characteristics and mechanical properties of Li-ion transport. The trajectory of Li-ions was collected for 30 ps while increasing T from 600 to 1200 K. The collected Li-ion trajectories were converted to Li-ion probability densities, as shown in Fig. 5a, where the grey shaded area indicates the probability density of Li-ions. Although LiBr was substituted, there was no difference in the probability density in the LPI3-Br series, indicating that the calculated glassy structure exhibited a similar trend in Li-ion conduction behaviours. To understand the effect of LiBr substitution on Li-ion transport characteristics in greater detail, the diffusivity (D) of Li-ions, D_{Li}, was calculated, as shown in Fig. 5b. Unlike the trajectories of Li-ion, we found that the effect of LiBr substitution is captured in D_{Li}, indicating Li-ion transport properties (Table S2, ESI†). The D_{Li} of LPI3-Br10 at 300 K was 3.24×10^{-9} cm^2 s^{-1}, which is approximately two or three times higher than that of other LPI3-Br series. In addition, it was confirmed that only LPI3-Br10 showed the highest σ_{ion} of 0.3 mS cm^{-1} and the lowest E_a of 0.21 eV among the LPI3-Br series (Fig. 5c). This suggests that the transport properties of Li-ions can be improved by tuning the halogen ions in the LPI3-Br series. The

mechanical properties of the LPI3-Br series were also extracted based on the DFT calculations using optimized glassy structures and compared with the results of the USPE technique, as shown in Fig. 5d. The calculated elastic constants of LPI3-Br series also showed similar trends, regardless of the LiBr substitution. In particular, the calculated E of LPI3-Br10 is 14.46 GPa, which is in good agreement with the experimentally measured result of 14.48 GPa. Therefore, we concluded that the Li-ion transport and mechanical properties of glassy SEs can be predicted through AIMD calculation, verifying that their atomic structures are well-reconstructed to reasonable statistical and experimental criteria.

Understanding of Li-ion transport and mechanical properties in LPI3-Br series

Through the structural mapping based on the results of RMC and AIMD methods, the mixed anions of the PS_4^{3-} molecular and halogen atomic ions can affect Li-ion transport and mechanical properties. To understand the Li-ion transport properties derived from the mixed anions composed of random PS_4^{3-} molecular and halogen atomic ions, we hypothesized an enhancement of Li-ion conduction in the LPI3-Br series, as shown in Fig. 6a. In the case of a single halogen-based glassy SE, Li-ions undergo steric hindrance while moving through the anion lattice due to the large ionic radius of I^- (1.15 Å). In contrast, the mixed halogen-based glassy SE enables easier Li-ion conduction due to the rattling of Br^- with a small ionic radius (0.94 Å). In addition, the substitution of a small amount of LiBr enables the vibration of Br ions without modifying the glass former, which can further accelerate Li-ion transport. As a result, the activated Li-ions can overcome a high activation barrier or migrate to new conduction pathways that had to be detoured. Based on this hypothesis, the variation in the coordination numbers of Li-S, Li-I, and Li-Br at T = 800 K was identified, confirming the effect of the mixed halogen ions on the Li-ion conduction characteristics, as shown in Fig. 6b. The average coordination numbers of Li-S and Li-I in LPI3 were 2.71 and 4.08, respectively, and they remained constant without significant change during the 30 ps calculation time. This

variation in the coordination number of the Br ion undergoes a large change with increasing LiBr content. The coordination number of the Li-Br ion in LPI3-Br5 changed significantly from two to six. As the LiBr content increased, the variation in the coordination number of Li-Br converged to that of Li-I. To understand the change in coordination number in the LPI3-Br series, the mean-square displacement (MSD) of the halogen, which is related to the vibration characteristics of halogen ions, was calculated, as shown in Fig. 6c. The calculated MSD of I^- for LPI3 decreased linearly with increasing LiBr content. Meanwhile, the MSD of Br^- showed similar behaviour to that of σ_{ion}. Coincidentally, the highest D of Br ions (1.02×10^{-7} cm^2 s^{-1}) was obtained for LPI3-Br10 with the highest σ_{ion}, indicating that the polarization of Br^- in the glass matrix can be further amplified (Table 3). From the variation of the coordination number and vibration characteristics, we confirmed that the substitution of a small amount of LiBr can accelerate Li-ion conduction by securing the conduction path and increase the vibration of the halogen ion in the glass network.

Conclusions

In this study, we reported new anion framework-controlled glassy sulfide SEs with fast Li-ion conduction and high deformability by employing combinatorial atomic analysis based on the PDF and RMC methods. The glassy sulfides with reasonable σ_{ion} and high deformability have been considered as one of the promising SEs for ASSBs. However, the limited understanding of glassy structures due to the absence of long-range ordering hampers accurate property control and design of novel structures. To make the glassy structure more prominent as a SE, the observation of anion locations and bond changes between ions is important for characterizing Li-ion transport and mechanical properties. Therefore, guidelines for synthesizing glassy SEs with high σ_{ion} and low E values using advanced techniques that can overcome the limitations of conventional bulk analyses are required. Here, we conceived a

novel glassy material with two halogens as atomic anions (Br^- and I^-) with intrinsic PS_4^{3-} molecular anions as a model study. First, σ_{ion} was measured by changing the composition of ternary LPI system to find the optimum glass matrix. Among the various glass matrices, LPI3, $[(Li_2S)_{0.658}(LiI)_{0.342}]_{0.825}[P_2S_5]_{0.175}$, was chosen due to its high σ_{ion}. Through halogen ion tuning by LiBr substitution in LPI3, LPI3-Br10 showed the highest σ_{ion} of 2.27 mS cm^{-1} and lowest E_a of 0.18 eV among the LPI3-Br series. In addition, we measured the mechanical properties of LPI3-Br series through the USPE technique. The E value of LPI3-Br10 was still suppressed to 14.48 GPa despite its high σ_{ion}, indicating that the mixed halogen in the glassy matrix can achieve high σ_{ion} without deterioration of mechanical properties. To confirm the changes in σ_{ion} and mechanical properties according to the distribution of mixed anion clusters, structural mapping of the LPI3-Br series was performed by introducing RMC simulation based on experimental PDF results. AIMD calculations were then performed to understand Li-ion conduction and mechanical properties based on the reconstructed glassy structure. In the glassy matrix of LPI3-Br10, Br-ions can easily change their coordination numbers and are highly vibrated. This indicates that the polarization of halogen ions can be maximized by substituting a small amount of LiBr. Our synthesis and analysis strategies based on mixed anions with two halogen ions will provide insights into the synthesis of SEs that require fast Li-ion conduction and high deformability. Furthermore, LPI3-Br10 with high σ_{ion} and low E values can be used as a promising glassy SE to control the deterioration of ASSBs in complex operating environments.

Materials and methods

Sample preparation

The starting materials, Li_2S (99.98%, Sigma-Aldrich), P_2S_5 (99%, Sigma-Aldrich), LiI (99.999%, Sigma-Aldrich), and LiBr (99.9%, Sigma-Aldrich), were placed in a ZrO_2 bowl and mixed in the appropriate stoichiometric ratio. 2.00 g mass of the mixtures were synthesized for the preparation of sulfide glassy SEs by mechanochemical milling (PM200, Retsch). Milling was conducted at 650 rpm for 12 h (milling: 30 min, pause: 30 min, cycle: 12). All samples were treated in a glove box and a sealed container filled with Ar gas (99.999%).

Structure characterization

The laboratory XRD patterns of all sulfide glassy SEs samples were obtained using an X-ray diffractometer (D8 Advance, Bruker) with Cu-Kα radiation (λ = 1.540598 Å). All laboratory XRD data were obtained over the 10–65° 2θ range in 0.02° steps. All samples were sealed with Kapton polyimide film to prevent air exposure and contamination. The σ_{ion} of the sulfide glassy SEs was measured using electrochemical interface equipment (Model 1287, Solartron) and a frequency response analyzer (Model 1260, Solartron) with an AC amplitude of 50 mV over a frequency range of 10–10^6 Hz. For measurement of σ_{ion} at room temperature on cold-pressed 6-mm-diameter pellets, about 0.2 g of powder was uniaxially pressed at 200 MPa. To obtain E_a, 0.2 g of sulfide glassy SE was placed in a mold of diameter 0.6 mm and then pressed at 200 MPa to prepare the pellet. Subsequently, the mold was placed in a heating jacket, and the temperature was decreased from 100 ° to 40 °C in 10 °C decrements (see Fig. S4, ESI†). At each temperature, σ_{ion} was measured after holding it for approximately 10 min. XPS (PHI 5000 VersaProbe, ULVAC PHI) using focused monochromatized Al Kα radiation (hv = 1486.6 eV) was performed to reveal the bonding characteristics of the LP and LPI series. The obtained binding energy was calibrated with the C 1*s* peak to 284.6 eV. The LP

and LPI series powders were placed on a sample holder in a dry Ar-filled glovebox and transferred to a chamber using a vacuum transfer vessel to avoid air exposure. The X-ray spot size was 100 μm × 100 μm, and the narrow scan pass energy was set to 58.7 eV. High-resolution scans were recorded in the P and S 2*p* energy regions with the pass energy.

Mechanical property measurement

The mechanical properties of the LPI3-Br series were measured using an ultrasonic pulse echo technique. The longitudinal and shear wave transducers were A127S-RM (10 MHz centre frequency) and V154-RM (2.25 MHz centre frequency), respectively. To obtain the sound speed of the longitudinal and shear waves, cold pressed 10-mm-diameter pellets were placed in the air protection holder and measured by 5072 PR (Olympus) as an RF receiver. The measurements of the longitudinal and shear waves were repeated at least five times (see Fig. S5, ESI†). Using the obtained V_L and V_S, E, B, G, and v were calculated using the following equations:

$$E = \rho V_S^2 \frac{(3 V_L^2 - 4V_S^2)}{(V_L^2 - V_S^2)}$$

$$G = \rho V_S^2$$

$$B = \rho \frac{(V_L^2 - 4/3 V_S^2)}{(V_L^2 - V_S^2)}$$

$$v = \rho \frac{(V_L^2 - 2 V_S^2)}{(2V_L^2 - 2V_S^2)}$$

where ρ is the density of sample.

Synchrotron X-ray PDF measurement

High energy total scattering images with X-ray energies of 74 keV (λ = 0.1665 Å) were obtained using a Perkin-Elmer amorphous silicon detector at 28-ID-1-PDF beamline, National Synchrotron Light Source II (NSLS-II) at Brookhaven National Laboratory.

Sample-to-detector distance (SDD) was about 213 mm. X-ray beam profile of 500 μm height × 500 μm width was used. A Nickel powder (catalog number: 10256, Alfa Aesar) in a Kapton tube (outer diameter = 1mm) was used to calibrate SDD. Integration of 2-dimensional (2D) scattering images into 1-D patterns was done using Dioptas software.[39] xPDFsuite program was used to obtain the PDF by Fourier transformation with a Q range of 0.1–20 $Å^{-1}$.[40]

Reverse Monte-Carlo simulation

Based on the experimental $S(q)$ obtained from the PDF measurements, the structural mapping of the LPI3-Br series was conducted using RMC simulation with the RMC++ code.[41,42] The cut-off distance was set using experimentally measured PDF, as listed in Table S1. The initial structure of the LPI3-Br series was composed of PS_4^{3-}, Li-, and halogen ions. The total number of atoms in glassy structure was 6480 in cubic cell. All RMC simulations were performed until less 5% R_w. To prevent the unintended generation of anion molecules in the LPI3-Br series, the coordination numbers between P and S of PS_4^{3-} and between P and P were set to four and one, respectively.

Density functional theory calculation

All calculations were performed using the Vienna *ab initio* simulation package (VASP) based on DFT.[43] The following is a summary of the DFT calculation settings used for the initial glassy structure optimization and mechanical properties of the LPI3 and LPI3-Br series; further details are provided in the reference.[44,45] The electron wave functions were described by the PAW method of Blöchl and implemented in the VASP by Kresse and Joubert.[46,47] The exchange correlation energy was described using the generalized gradient approximation of Perdew, Burke, and Ernzerhof.[48,49] The wave functions were expanded in plane waves with a cut-off energy of 520 eV. Partial wave occupancies were calculated using the Gaussian

smearing method with a smearing width of 0.05 eV. All images were drawn using Visualization for Electronic and STructural Analysis software.[50]

The Li-ion transport characteristics of the LPI3-Br series were obtained using AIMD calculations based on DFT. Based on the glassy structure obtained by RMC calculations, a glass structure containing 230 atoms with ρ of 2.1 g cm^{-3} were constructed and simulated with canonical ensemble using a Nosé–Hoover thermostat. As previously reported, the γ-point-only k-point mesh and cut-off energy of 280 eV were used in all AIMD calculation due to limited computational cost. The initial structure was equilibrated from 500 to 500 K for 20 ps and then cooled to 300 K for 10 ps (cooling rate = 20 K ps^{-1}). The time step was set to 2 fs, as recommended in the literature.[45,51] To understand the Li-ion conduction behavior of the LPI3-Br series, transport properties of Li-ion, such as probability density, MSD, and D, were obtained using pymatgen-diffusion code, as implemented in Python Materials Genomics code.[52] D of each atom was calculated using the following equation:

$$D = \frac{1}{2dt}\langle[\Delta r(t)^2]\rangle$$

where d is the dimension factor, which was set to three, and $\langle[\Delta r(t)]^2\rangle$ is the average MSD over a time duration t (see Fig. S6, ESI†). The calculated D_{Li} of LPI3 and LPI3-Br series are listed in Table S2. Through the calculated D_{Li} of the LPI3-Br series, σ_{ion} at room temperature was calculated using following equation:

$$\sigma_{\mathrm{ion}} = \frac{c_{\mathrm{ion}}(q_{\mathrm{ion}}e)^2}{k_{\mathrm{B}}T}D_{\mathrm{Li}}$$

where c_{ion} is the Li-ion concentration in the glassy structure, q_{ion} is the formal charge of the Li-ion, e is the elementary charge, and k_B is the Boltzmann constant. The range of T was set from 600 to 1200 K.

Author contributions

The project was conceived by J.S.K. and H.K. Sample preparation and property measurement were carried out by J.S.K., Y.J.K., H.G.J., B.K.K., K.J.Y., and H.K. High energy X-ray scattering measurements and analyses were performed by J.S.K., D.H., K.W.N., G.K., and H.K. The computational works and analyses were performed by J.S.K., T.W.H., and H.K. The manuscript was written by J.S.K. and H.K. All authors discussed the results and commented on the manuscript.

Competing interests

The authors declare no competing interests.

Acknowledgements

This work was supported by the National Research Foundation of Korea (NRF) grant funded by the Korea government (MSIT) (No.2020R1A2C2010191). This work was partly supported by the Development Program of Core Industrial Technology, funded by the Ministry of Trade, Industry & Energy of Korea (No. 20012318). This work was also supported in part by the Institutional Research Program of the Korea Institute of Science and Technology (2E31852). Part of this work was performed under the auspices of the U.S. Department of Energy by Lawrence Livermore National Laboratory (LLNL) under Contract DE-AC52-07NA27344. The PDF research used beamline 28-ID-1 of the National Synchrotron Light Source II, a US Department of Energy (DOE) Office of Science User Facility operated for the DOE Office of Science by Brookhaven National Laboratory under contract no. DE-SC0012704.

References

1. M. D. Ingram, *Curr. Opin. Solid State Mater. Sci.,*1997*,* **2**, 399–404.
2. S. Kohara, K. Suzuya, K. Takeuchi, C.-K. Loong, M. Grimsditch, J. K. R. Weber, J. A. Tangeman and T. S. Key, *Science*, 2004, **303**, 1649–1652.
3. G. N. Greaves and S. Sen, *Adv. Phys.,* 2007, **56**, 1–166.
4. T. Rouxel, *J. Am. Ceram. Soc*., 2007, **90**, 3019–3039.
5. A. Ananthanarayanan, G. Tricot, G. P. Kothiyal and L. Montagne, *Crit. Rev. Solid State Mater. Sci*., 2011, **36**, 229–241.
6. M. Edén, *Ann. Rep. Prog. Chem., Sec. C*, 2012, **108**, 177–221.
7. Z.-H. Jiang and Q.-Y. Zhang, *Prog. Mater. Sci.*, 2014, **61**, 144–215.
8. J. C. Mauro, *Front. Mater.*, 2014, **1***,* 20.
9. J. W. Yu, S. H. E Rahbari, T. Kawasaki, H. Park and W. B. Lee, *Sci. Adv.*, 2020, **6**, eaba8766.
10. H. Hosono, J. Kim, Y. Toda, T. Kamiya and S. Watanabe, *Proc. Natl. Acad. Sci.*, 2017, **114**, 233–238.
11. E. J. Frankberg, J. Kalikka, F. G. Ferré, L. Joly-Pottuz, T. Salminen, J. Hintikka1, M. Hokka, S. Koneti, T. Douillard, B. L. Saint, P. Kreiml, M. J. Cordill, T. Epicier, D. Stauffer, M. Vanazzi, L. Roiban, J. Akola, F. D. Fonzo, E. Levänen and K. Masenelli-Varlot, *Science*, 2019, **366**, 864–869.
12. J. N. Mundy, *Solid State Ionics*, 1988, **28–30**, 671–676.
13. J. L. Souquet, *Ann. Rev. Mater. Sci.*, 1981, **11**, 211–231.
14. H. Lou, Z. Zeng, F. Zhang, S. Chen, P. Luo, X. Chen, Y. Ren, V. B. Prakapenka, C. Prescher, X. Zuo, T. Li, J. Wen, W.-H. Wang, H. Sheng and Q. Zeng, *Nat. Comm.*, 2020, **11**, 314.

15. A. Hirata, P. Guan, T. Fujita, Y. Hirotsu, A. Inoue, A. R. Yavari, T. Sakurai and M. W. Chen, *Nat. Mater.*, 2011, **10**, 28–33.
16. R. Mercier, J. P. Malugani, B. Fahys and G. Robert, *Solid State Ionics*, 1981, **5**, 663-666.
17. M. Tatsumisago and A. Hayashi, *Solid State Ionics*, 2012, **225**, 342–345.
18. A. Sakuda, A. Hayashi and M. Tatsumisago, *Sci. Rep.*, 2013, **3**, 2261.
19. A. Kato, M. Yamamoto, A. Sakuda, A. Hayashi and M. Tatsumisago, *ACS Appl. Energy Mater.*, 2018, **1**, 1002–1007.
20. Z. A. Grady, C. J. Wilkinson, C. A. Randall and J. C. Mauro, *Front. Energy Res.*, 2020, **8**, 218.
21. S. Wang, W. Zhang, X. Chen, D. Das, R. Ruess, A. Gautam, F. Walther, S. Ohno, R. Koerver, Q. Zhang, W. G. Zeier, F. H. Richter, C. W. Nan and J. Janek, *Adv. Energy Mater.*, 2021, **11**, 2100654.
22. M. G. Boebinger, D. Yeh, M. Xu, B. C. Miles, B. Wang, M. Papakyriakou, J. A. Lewis, N. P. Kondekar, F. J. Q. Cortes, S. Hwang, X. Sang, D. Su, R. R. Unocic, S. Xia, T. Zhu and M. T. McDowell, *Joule*, 2018, **2**, 1783.
23. Y.-K. Sun, *ACS Energy Lett.*, 2020, **5**, 3221–3223.
24. A. Banerjee, X. Wang, C. Fang, E. A. Wu and Y. S. Meng, *Chem. Rev.*, 2020, **120**, 6878–6933.
25. R. Koerver, W. Zhang, L. de Biasi, S. Schweidler, A. O. Kondrakov, S. Kolling, T. Brezesinski, P. Hartmann, W. G. Zeier and J. Janek, *Energy Environ. Sci.*, 2018, **11**, 2142–2158.
26. I. Štich, R. Car and M. Parrinello, *Phys. Rev. B*, 1991, **44**, 11092–11104.
27. N. C. Cooper, C. M. Goringe and D. R. McKenzie, *Comput. Mater. Sci.*, 2000, **17**, 1–6.

28. C. Dietrich, D. A. Weber, S. J. Sedlmaier, S. Indris, S. P. Culver, D. Walter, J. Janek and W. G. Zeier, *J. Mater. Chem. A,* 2017, **5**, 18111−18119.
29. C. Dietrich, R. Koerver, M. W. Gaultois, G. Kieslich, G. Cibin, J. Janek and W. G. Zeier, *Phys. Chem. Chem. Phys.*, 2018, **20**, 20088−20095.
30. W. D. Jung, B.-N. Yun, H.-G. Jung, S. Choi, J.-W. Son, J.-H. Lee, J. H. Lee and H. Kim, *APL Mater.,* 2018, **6**, 047902.
31. Y. Wang, W. D. Richards, S. P. Ong, L. J. Miara, J. C. Kim, Y. Mo and G. Ceder, *Nat. Mater.*, 2015, **14**, 1026–1031.
32. A. D. Sendek, G. Cheon, M. Pasta and E. J. Reed, *J. Phys. Chem. C*, 2020, **124**, 8067–8079.
33. Z. Xu, X. Chen, R. Chen, X. Li and H. Zhu, *NPJ Comput. Mater.*, 2020, **6**, 47.
34. M. Jansen, *Angew. Chem. Int. Ed. Engl.*, 1991, **30**, 1547–1558.
35. Z. Zhang, H. Li, K. Kaup, L. Zhou, P. N. Roy and L. F. Nazar, *Matter*, 2020, **2**, 1667–1684.
36. Z. Deng, Z. Wang, I.-H. Chu, J. Luo and S. P. Ong, *J. Electrochem. Soc.*, 2016, **163***,* A67–A74.
37. S. Muy, R. Schlem, Y. Shao-Horn and W. G. Zeier, *Adv. Energy Mater.*, 2021, **11**, 2002787.
38. N. Suzuki, W. D. Richards, Y. Wang, L. J. Miara, J. C. Kim, I.-S. Jung, T. Tsujimura and G. Ceder, *Chem. Mater.*, 2018, **30**, 2236–2244.
39. A. Prescher and V. B. Prakapenka, *High Pressure Res.*, 2015, **35**, 223–230.
40. X. Yang, P. Juhas, C. L. Farrow and S. J. Billinge, arXiv preprint arXiv:1402.3163, 2014.
41. R. L. McGreevy and L. Pusztai, *Mol. Simul.*, 1988, **1**, 359–367.
42. R. L. McGreevy, *J. Phys. Condens. Matter,* 2001, **13**, R877–R913.

43. G. Kresse and J. Furthmüller, *Comput. Mater. Sci.*, 1996, **6**, 15–50.
44. J.-S. Kim, W. D. Jung, S. Choi, J.-W. Son, B.-K. Kim, J.-H. Lee and H Kim, *J. Phys. Chem. Lett.*, 2018, **9**, 5592–5597.
45. J.-S. Kim, W. D. Jung, J.-W. Son, J.-H. Lee, B.-K Kim, K.-Y. Chung, H.-G. Jung and H. Kim, *ACS Appl. Mater. Interfaces*, 2019, **11**, 13−18.
46. G. Kresse and J. Furthmüller, *Phys. Rev. B*, 1996, **54**, 11169–11186.
47. P. E. Blochl, *Phys. Rev. B*, 1994, **50**, 17953–17979.
48. G. Kresse and D. Joubert, *Phys. Rev. B*, 1999, **59**, 1758–1775.
49. P. Perdew, K. Burke and M. Ernzerhof, *Phys. Rev. Lett.*, 1996, **77**, 3865–3868.
50. K. Momma and F. Izumi, *J. Appl. Crystallogr.*, 2008, **41**, 653–658.
51. W. D. Richards, Y. Wang, L. J. Miara, J. C. Kim and G. Ceder, *Energy Environ. Sci.*, 2016, **9**, 3272–3278.
52. S. P. Ong, W. D. Richards, A. Jain, G. Hautier, M. Kocher, S. Cholia, D. Gunter, V. Chevrier, K. A. Persson and G. Ceder, *Comp. Mater. Sci.*, 2013, **68**, 314–319.

Figure legends

Fig. 1 Conventional LPI glass framework. (a) Schematic illustration of glass formers in glassy SEs. The glass formers in sulfide SEs can be composed of monatomic, diatomic, and molecular clusters. (b) Schematic illustration of proposed two Li-ion migration mechanism in glass framework: hopping (blue circle, left) and paddle wheel (red circle, right) mechanisms. (c) Contour ternary diagram showing the relationship between σ_{ion} and the normalized composition of the LP and LPI series. The grey stars indicate the LP75 and LPI series. (d) Laboratory XRD patterns of LP75 and LPI series. (e) P_{2p} (left) and S_{2p} (right) XPS spectra of LP75 and LPI series. The red and blue areas represent PS_4^{3-} and $P_2S_6^{2-}$, respectively.

Fig. 2 Effect of LiBr substitution on Li-ion transport properties. (a) Laboratory XRD patterns of LPI3-Br series. (b) Variations in σ_{ion} at room temperature for LPI3-Br series. (c) Arrhenius relationship of σ_{ion} in LPI3-Br series. The measured results of conventional glassy SEs (LPI75 and LPI3) are also shown for comparison purpose. Values in parentheses indicate the E_a of each sample.

Fig. 3 Mechanical properties of LPI3-Br series. (a) Variation of various elastic constants (E, G, and B) and v in LPI3-Br series. The measured elastic constants and related information used for USPE method are also summarized in Table 2. (b) Comparison of E (left) and σ_{ion} (right) between reported sulfide SEs and LPI3-Br10. The E of LP series materials were reported both experimentally and theoretically.[19,36]

Fig. 4 Structural mapping of LPI3-Br series using RMC simulation. (a) $S(q)$ and (b) $g(r)$ of LPI3-Br series using synchrotron X-ray-based PDF and RMC methods. The accuracy of the refined structural models was evaluated using the R_w fit indicator. The narrow panel (right) in

$g(r)$ shows the short-range ordering in detail by magnifying the lower distance region. (c) Distribution of Li, halogen, and PS_4^{3-} tetrahedron in LPI3-Br series. Lower circle images show the magnified view of ion distribution.

Fig. 5 Prediction of Li-ion transport and mechanical properties in LPI3-Br series using AIMD calculation. (a) Li-probability density of LPI3-Br series. The grey area indicates the Li-ion probability density. (b) Arrhenius relationship of D_{Li} in LPI3-Br series. (c) Comparison of σ_{ion} and E_a of LPI3-Br series. (d) Calculated elastic constants (E, G, and B) and v of LPI3-Br series.

Fig. 6 Effect of mixed halogen ions on Li-ion conduction characteristic in LPI3-Br series. (a) Schematic illustration of Li-ion conduction mechanism in single and mixed halogen ions in sulfide glass. Variations in the (b) coordination number and (c) MSD of halogen ions for LPI3-Br series. MSD results for Br and I ions in LPI3-Br series were obtained from their AIMD trajectories at 800 K. The detailed data are presented in Table 3.

Figures

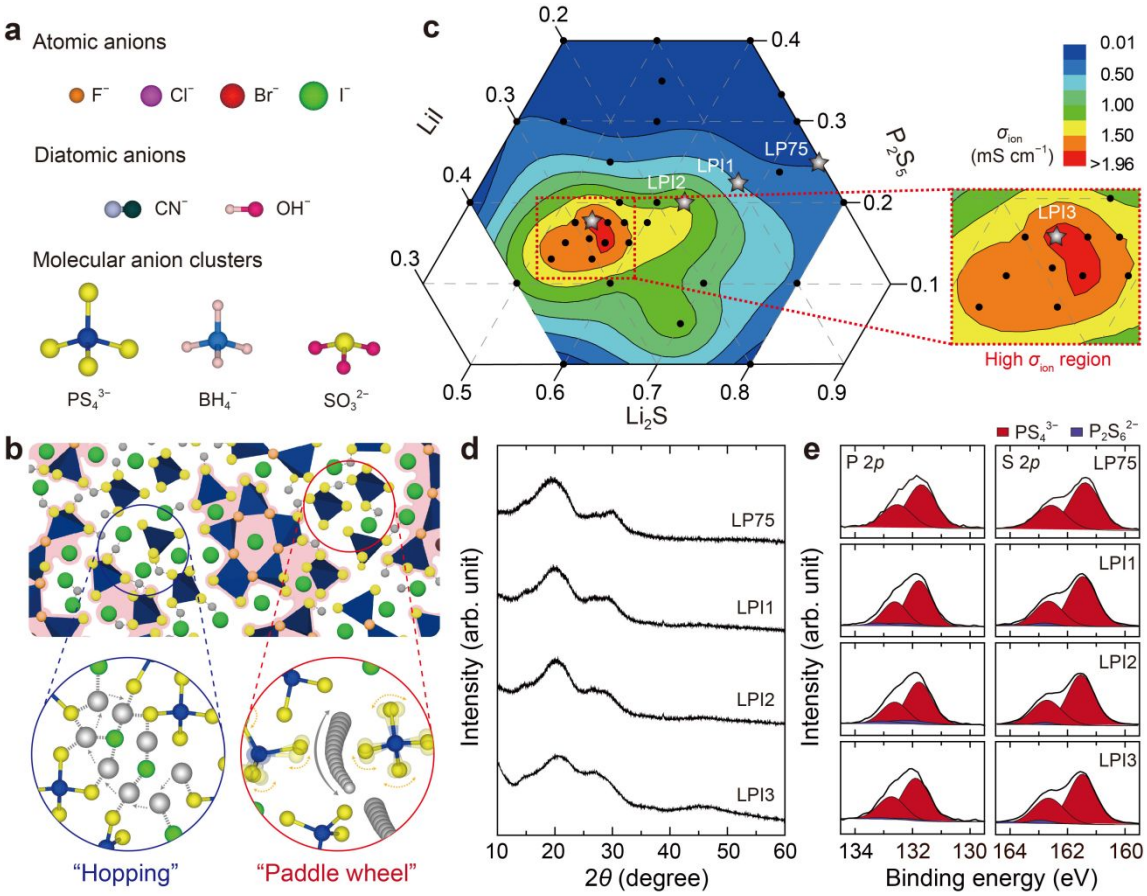

Figure 1

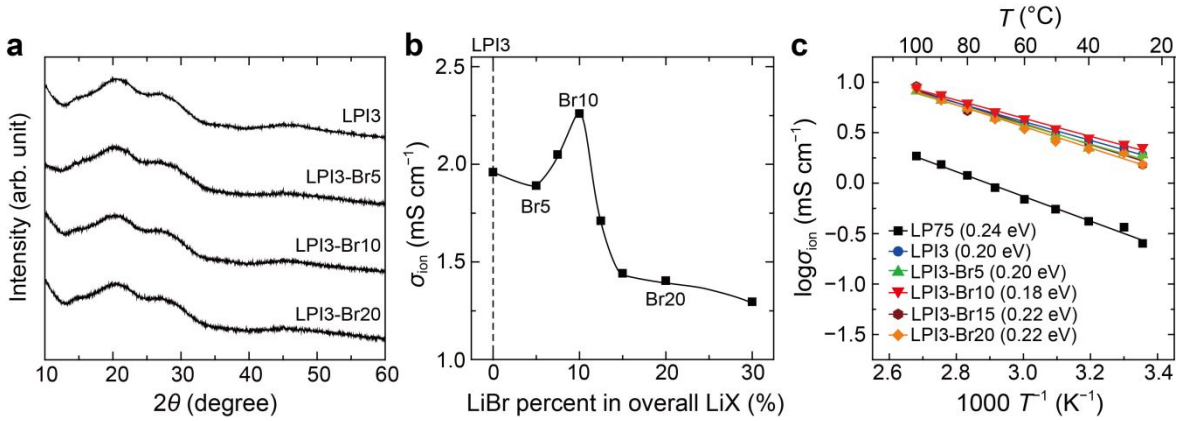
a
Intensity (arb. unit)
LPI3
LPI3-Br5
LPI3-Br10
LPI3-Br20
10 20 30 40 50 60
2θ (degree)
b
LPI3
Br10
Br5
Br20
σion (mS cm−1)
2.5 2.0 1.5 1.0
0 10 20 30
LiBr percent in overall LiX (%)
c
T (°C)
100 80 60 40 20
logσion (mS cm−1)
1.0 0.5 0.0 −0.5 −1.0 −1.5
LP75 (0.24 eV)
LPI3 (0.20 eV)
LPI3-Br5 (0.20 eV)
LPI3-Br10 (0.18 eV)
LPI3-Br15 (0.22 eV)
LPI3-Br20 (0.22 eV)
2.6 2.8 3.0 3.2 3.4
1000 T−1 (K−1)

Figure 2

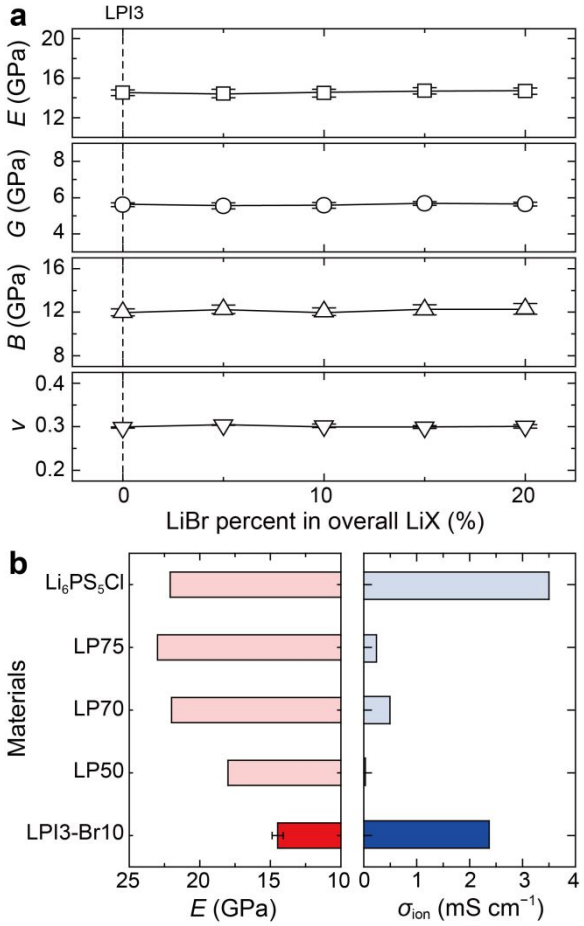
a
LPI3
E (GPa)
G (GPa)
B (GPa)
v
LiBr percent in overall LiX (%)
b
Materials
Li6PS5Cl
LP75
LP70
LP50
LPI3-Br10
E (GPa)
σion (mS cm−1)

Figure 3

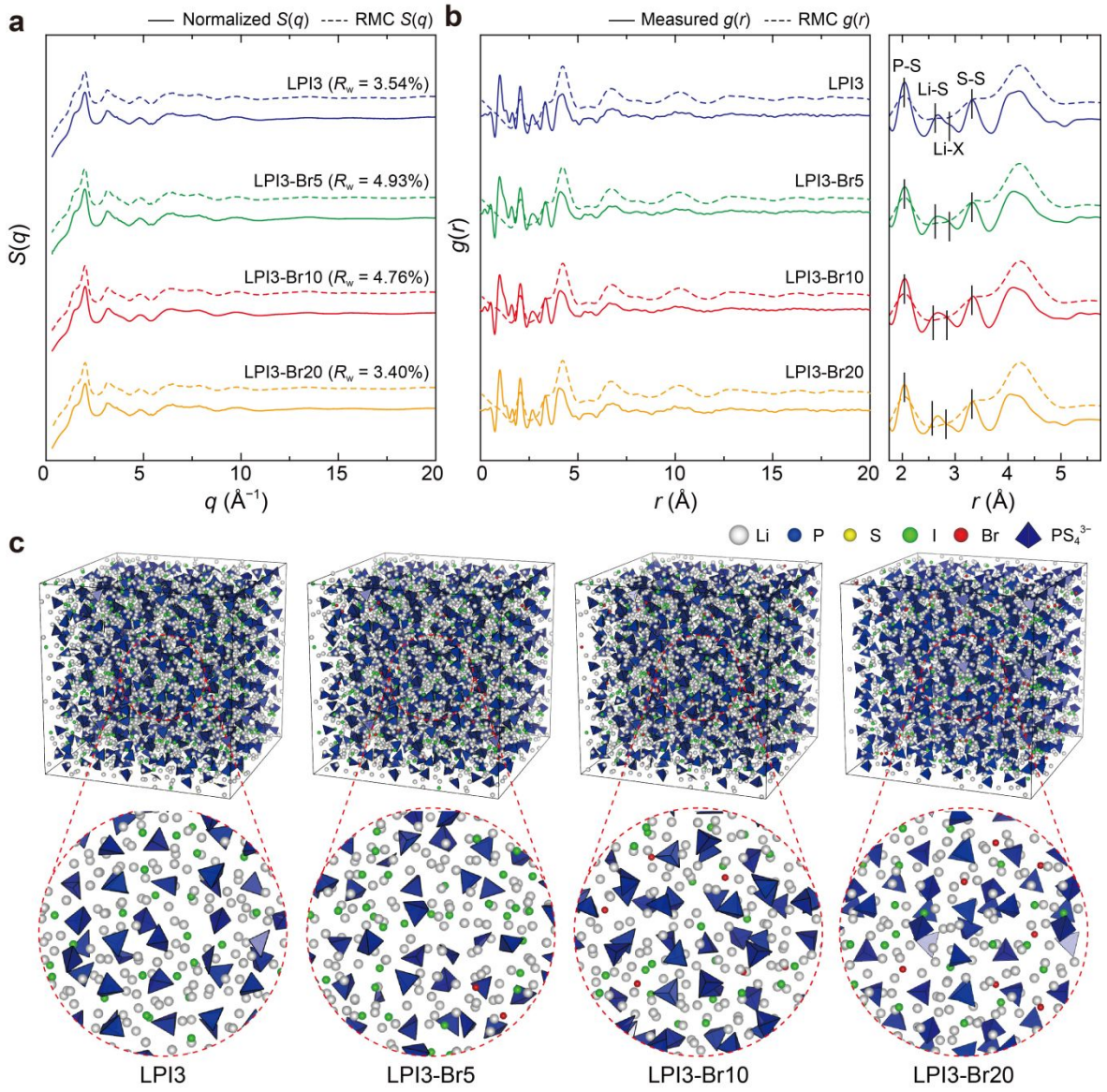
a
Normalized S(q) RMC S(q)
LPI3 (Rw = 3.54%)
LPI3-Br5 (Rw = 4.93%)
LPI3-Br10 (Rw = 4.76%)
LPI3-Br20 (Rw = 3.40%)
S(q)
q (Å−1)
b
Measured g(r) RMC g(r)
LPI3
LPI3-Br5
LPI3-Br10
LPI3-Br20
g(r)
r (Å)
P-S
Li-S
S-S
Li-X
c
Li P S I Br PS4 3−
LPI3
LPI3-Br5
LPI3-Br10
LPI3-Br20

Figure 4

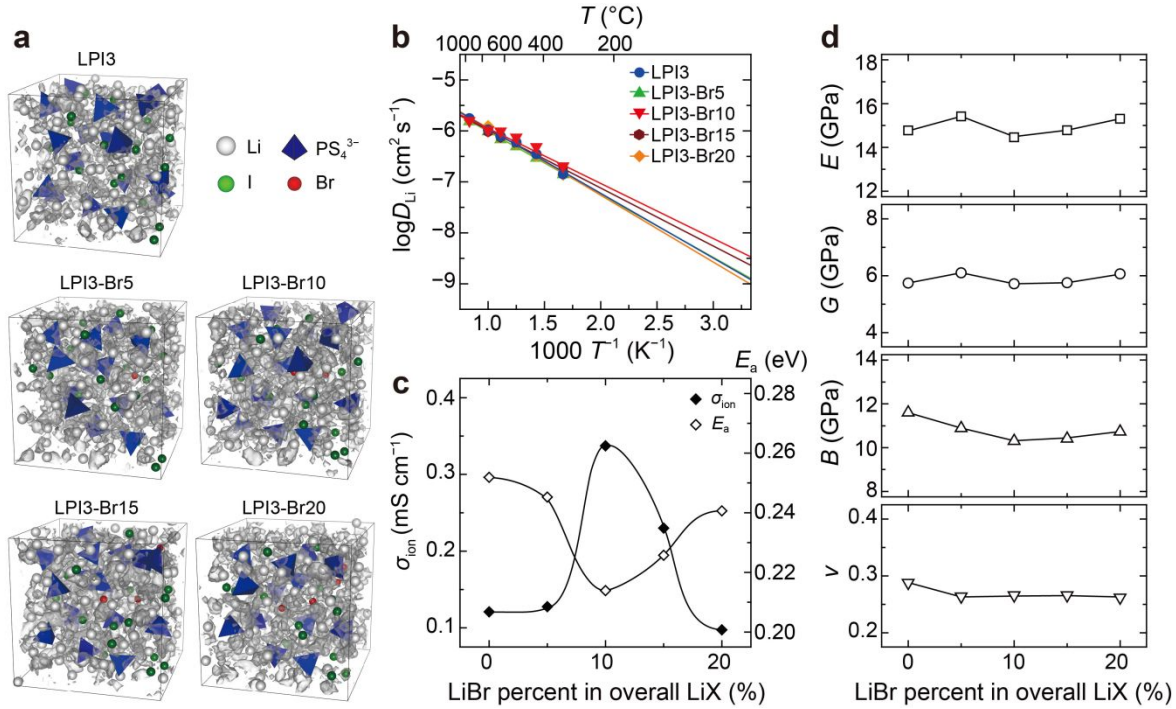
a
LPI3
Li
PS_4^{3-}
I
Br
LPI3-Br5
LPI3-Br10
LPI3-Br15
LPI3-Br20
b
T (°C)
1000 600 400 200
LPI3
LPI3-Br5
LPI3-Br10
LPI3-Br15
LPI3-Br20
$\log D_{Li}$ ($cm^2 s^{-1}$)
1000 T^{-1} (K^{-1})
c
σ_{ion}
E_a
σ_{ion} (mS cm^{-1})
E_a (eV)
LiBr percent in overall LiX (%)
d
E (GPa)
G (GPa)
B (GPa)
ν
LiBr percent in overall LiX (%)

Figure 5

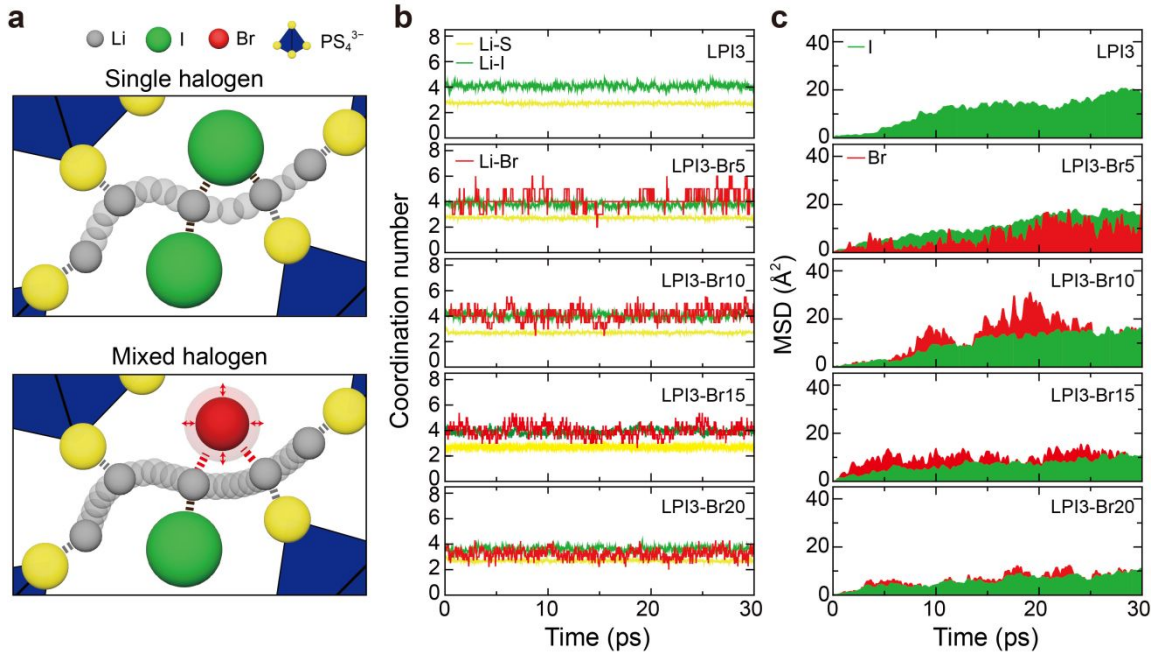
a
Li
I
Br
PS_4^{3-}
Single halogen
Mixed halogen
b
Li-S
Li-I
Li-Br
LPI3
LPI3-Br5
LPI3-Br10
LPI3-Br15
LPI3-Br20
Coordination number
Time (ps)
c
I
Br
LPI3
LPI3-Br5
LPI3-Br10
LPI3-Br15
LPI3-Br20
MSD (Å^2)
Time (ps)

Figure 6

Table legends

Table 1 Detailed information on various glassy sulfide SEs tested in this study. Acronym, chemical formula, σ_{ion} and E_a in LPI, LPI3-Br series, and reported sulfide based glass SEs.

Table 2 Measured mechanical properties in LPI3-Br series using the USPE method. The ρ is the sample density. Values in parentheses indicate the standard deviation.

Table 3 Vibration characteristics of halogen ions in LPI3-Br series. The avergage coordination number and D_X (X = Br or I) were obtained at T = 800 K.

Tables

Table 1

Acronym	Chemical formula	σ_{ion} (mS cm^{-1}))	E_a (eV)
LPI1	$[(Li_2S)_{0.871}(LiI)_{0.129}]_{0.775}[P_2S_5]_{0.225}$	0.67	-
LPI2	$[(Li_2S)_{0.813}(LiI)_{0.183}]_{0.800}[P_2S_5]_{0.200}$	1.26	-
LPI3	$[(Li_2S)_{0.658}(LiI)_{0.342}]_{0.825}[P_2S_5]_{0.175}$	1.96	0.20
LPI3-Br5	$[(Li_2S)_{0.658}(LiI_{0.95}LiBr_{0.05})_{0.342}]_{0.825}[P_2S_5]_{0.175}$	1.89	0.20
LPI3-Br10	$[(Li_2S)_{0.658}(LiI_{0.90}LiBr_{0.10})_{0.342}]_{0.825}[P_2S_5]_{0.175}$	2.27	0.18
LPI3-Br15	$[(Li_2S)_{0.658}(LiI_{0.85}LiBr_{0.15})_{0.342}]_{0.825}[P_2S_5]_{0.175}$	1.44	0.22
LPI3-Br20	$[(Li_2S)_{0.658}(LiI_{0.80}LiBr_{0.20})_{0.342}]_{0.825}[P_2S_5]_{0.175}$	1.40	0.22
LP75	$(Li_2S)_{0.75}(P_2S_5)_{0.25}$	0.25	0.24
LP70	$(Li_2S)_{0.70}(P_2S_5)_{0.30}$	0.48	-
LP50	$(Li_2S)_{0.50}(P_2S_5)_{0.50}$	0.001	-

Table 2

Sample	ρ (g cm^{-3})	V_L (m s^{-1})	V_S (m s^{-1})	v	E (GPa)	G (GPa)	B (GPa)
LPI3	2.11	3033 (36)	1690 (15)	0.298 (0.001)	14.53 (0.29)	5.60 (0.11)	11.98 (0.32)
LPI3-Br5	2.10	3068 (48)	1593 (24)	0.304 (0.001)	14.44 (0.43)	5.54 (0.17)	12.26 (0.40)
LPI3-Br10	2.12	3141 (42)	1646 (22)	0.306 (0.001)	14.48 (0.39)	5.57 (0.15)	12.04 (0.36)
LPI3-Br15	2.10	3069 (48)	1627 (16)	0.299 (0.001)	14.72 (0.32)	5.67 (0.11)	12.23 (0.47)
LPI3-Br20	2.13	3051 (50)	1624 (16)	0.302 (0.04)	14.63 (0.32)	5.62 (0.11)	12.30 (0.50)

Table 3

Sample	Average coordination number			D_X (10^{-7} cm^2 s^{-1})	
	Li-S	Li-I	Li-Br	I	Br
LPI3	2.71	4.08	-	1.02	-
LPI3-Br5	2.72	3.80	4.17	0.93	0.98
LPI3-Br10	2.70	4.05	4.21	0.93	1.02
LPI3-Br15	2.68	3.98	3.98	0.43	0.62
LPI-Br20	2.70	3.61	3.24	0.40	0.40